Biofabrication

International Society
for Biofabrication

PAPER • OPEN ACCESS

On-chip high-definition bioprinting of microvascular structures

To cite this article: Agnes Dobos *et al* 2021 *Biofabrication* **13** 015016

IOP Publishing *Biofabrication* **13** (2021) 015016 https://doi.org/10.1088/1758-5090/abb063

Biofabrication

CrossMark

OPEN ACCESS

RECEIVED
11 February 2020

REVISED
3 August 2020

ACCEPTED FOR PUBLICATION
18 August 2020

PUBLISHED
12 December 2020

PAPER

On-chip high-definition bioprinting of microvascular structures

Agnes Dobos[1,2], **Franziska Gantner**[1,2], **Marica Markovic**[1,2], **Jasper Van Hoorick**[3,4], **Liesbeth Tytgat**[3,4],
Sandra Van Vlierberghe[3,4] and **Aleksandr Ovsianikov**[1,2,5]

[1] 3D Printing and Biofabrication Group, Institute of Materials Science and Technology, Technische Universität Wien (TU Wien), Vienna, Austria
[2] Austrian Cluster for Tissue Regeneration (http://tissue-regeneration.at), Austria
[3] Polymer Chemistry and Biomaterials Group, Centre of Macromolecular Chemistry, Ghent University, Ghent, Belgium
[4] Brussels Photonics, Department of Applied Physics and Photonics, Flanders Make and Vrije Universiteit Brussel, Brussels, Belgium
[5] Author to whom any correspondence should be addressed.

E-mail: Aleksandr.Ovsianikov@tuwien.ac.at

Keywords: multiphoton lithography, high-resolution bioprinting, thiol-ene chemistry, hydrogels, organ-on-chip, vascularization, microfluidic

Supplementary material for this article is available online

Abstract

'Organ-on-chip' devices which integrate three-dimensional (3D) cell culture techniques with microfluidic approaches have the capacity to overcome the limitations of classical 2D platforms. Although several different strategies have been developed to improve the angiogenesis within hydrogels, one of the main challenges in tissue engineering remains the lack of vascularization in the fabricated 3D models. The present work focuses on the high-definition (HD) bioprinting of microvascular structures directly on-chip using two-photon polymerization (2PP). 2PP is a nonlinear process, where the near-infrared laser irradiation will only lead to the polymerization of a very small volume pixel (voxel), allowing the fabrication of channels in the microvascular range (10–30 μm in diameter). Additionally, 2PP not only enables the fabrication of sub-micrometer resolution scaffolds but also allows the direct embedding of cells within the produced structure. The accuracy of the 2PP printing parameters were optimized in order to achieve high-throughput and HD production of microfluidic vessel-on-chip platforms. The spherical aberrations stemming from the refractive index mismatch and the focusing depth inside the sample were simulated and the effect of the voxel compensation as well as different printing modes were demonstrated. Different layer spacings and their dependency on the applied laser power were compared both in terms of accuracy and required printing time resulting in a 10-fold decrease in structuring time while yielding well-defined channels of small diameters. Finally, the capacity of 2PP to create vascular structures within a microfluidic chip was tested with two different settings, by direct embedding of a co-culture of endothelial- and supporting cells during the printing process and by creating a supporting, cell-containing vascular scaffold barrier where the endothelial cell spheroids can be seeded afterwards. The functionality of the formed vessels was demonstrated with immunostaining of vascular endothelial cadherin (VE-Cadherin) endothelial adhesion molecules in both static and perfused culture.

1. Introduction

Three-dimensional (3D) cell culture models that have the capacity to recapitulate the biochemical functionalities, mechanical properties and the microarchitecture of organs have been gaining increasing attention in biomedical research. These systems could provide more insights into the pathological and physiological functions of tissues compared to 2D cell cultures [1, 2]. 'Organ-on-chip' devices which integrate 3D cell culture techniques with microfluidic approaches could deliver an important platform to further improve *in vitro* organ and disease models [3, 4].

Several different polymers have been developed to home cells in 3D cell cultures, including nature-derived hydrogels and synthetic materials [2, 5, 6]. Natural hydrogels are physically or chemically cross-linked polymer networks which can take up large quantities of water without dissolving [6, 7]. They are often derived from the non-cellular compartment of the tissues called the extracellular matrix (ECM) [8]. Some of the commonly used ECM derived hydrogels include collagen [9–12], gelatin [13–16] and hyaluronic acid [12, 17]. The advantages of such materials include good biocompatibility, biodegradability and they often possess cell-responsive functionalities [5]. However, one of the main challenges in the use of such materials for biofabrication purposes includes the lack of control over the material properties due to the absence of (photo-)crosslinkable functional groups. Therefore, several different approaches have been developed to introduce reactive groups including (meth)acryloyl or thiol-ene functionalities to create networks following a chain- or step-growth polymerization [15]. Thiol-ene based step-growth polymerization offers several advantages over the more traditional chain-growth hydrogels, such as the lack of oxygen inhibition and faster reaction kinetics enabling the reproducible production of 3D printed structures with high structural integrity at low light intensities [18].

Although many different strategies have been developed to create biomimetic cell environments, one of the main challenges in tissue engineering and organ-on-chip devices remains the lack of vascularization in the fabricated 3D models [19, 20]. The vast majority of tissues in the body depend on blood vessels to supply nutrients and oxygen to the cells as the diffusion limit for oxygen is approximately 100–200 μm [21]. Microcirculation, based on the microvasculature, is the distal functional unit of the vascular system. The microvascular system consists of vessels with different diameters including the arterioles ($\pm$ 30 μm), venules ($\pm$ 20 μm) and capillaries ($<$ 8 μm) [22, 23]. Capillaries and venules are formed only by endothelial cells while arterioles also contain an additional layer of smooth muscle cells [23]. Tissues larger than a few hundred micrometres require the formation of new blood vessels by vasculogenesis and/or angiogenesis to supply the metabolic needs of the cells. Vasculogenesis is by definition the differentiation of a stem cell, precursor or angioblast while angiogenesis describes the process of remodelling and expansion where new vessels sprout from the already existing ones [24].

There are multiple different approaches which have been developed to increase the vascularization of a tissue construct. Previous studies showed that the scaffold design including the provided pore size and degradability is crucial for the formation of a neovascular network [25, 26]. The use of a supporting cell line co-cultured with endothelial cells also showed improved vascularization compared to a monoculture of endothelial cells. Supporting cells can be primary cells or cell lines including fibroblasts [27], hepatocytes [28], adipose derived stem cells [29], mesenchymal stem cells [30] or other cell types [31].

There are several different ways how 3D vascular structures could be created inside the microfluidic chips [32]. One of the most widespread approaches are using a template (sacrificial) material, needles or rods during the channel production which could be removed at a later time point leaving a hollow channel to be seeded with endothelial cells [33, 34].

Bioprinting can provide a valuable toolset to engineer vascularized tissue and organ-on-chip models [35]. These constructs can be fabricated using two main tissue engineering approaches either using a scaffold-based [36, 37] or bottom-up (BU) technology [38–40]. In scaffold-based bioprinting, cells are either seeded or embedded in a bioink matrix, while in BU bioprinting usually cell-spheroids are used without any scaffold support. Although these approaches can provide a promising strategy to form neovascularized tissue models, they often lack the resolution to create channels in the microvascular range (under 30 μm).

To circumvent this drawback, high resolution additive manufacturing techniques including two-photon polymerization (2PP) can be applied. 2PP is a nonlinear process where a near-infrared laser pulse is absorbed by a photosensitive material. In this respect, polymerization will only occur in the area where the photon density is high enough to result in simultaneous absorption of two or more photons, each carrying part of the required energy to pass the band gap [40, 41]. As a consequence, this method does not require layer-by-layer deposition of the material and the structures can be written directly within the volume of the sample. Additionally, by controlling the light dose, resolution under the diffraction limit can be achieved by polymerizing a small volume pixel (voxel). Furthermore, photopolymerization can proceed under relatively mild reaction conditions, enabling the direct embedding of cells within the bioink [42]. The accuracy of the 2PP produced structures mainly depends on the voxels and their arrangement [43].

The present work focuses on 2PP of microvascular structures directly on-chip using a thiol-ene photo-click hydrogel consisting of thiolated gelatin (Gel-SH) and gelatin-norbornene (Gel-NB). In order to demonstrate the ability of the employed material to support the spontaneous formation of vascular structures, a UV-induced (single-photon) encapsulation co-culture of human umbilical vein endothelial cells (HUVEC) with adipose derived stem cells (ASC/TERT1) was performed. This setting also allows to address the network forming capacity of the

HUVECs spheroids compared to single cell suspensions. In order to direct the alignment of HUVECs into vascular structures with various diameters resembling the diameters of the natural microvasculature, gelatin-based microvascular units were structured in the same material using 2PP. The accuracy of the 2PP printing can be affected by spherical aberrations resulting from refractive index (RI) mismatch and focusing depth. The printing parameters were optimized to increase the throughput and precision of the system accounting for voxel size and different printing modes. To further demonstrate the capabilities of this technology, two different approaches were explored: direct encapsulation of HUVECs spheroids into single microvascular units surrounded by the supporting cells, and the seeding of the endothelial cell spheroids into a microvascular barrier structure containing only the supporting cell line. The cell alignment was followed over 5 days via laser scanning confocal microscopy (LSM) in static and perfused culture and finally, the intercellular junctions were immuno-stained using an anti-vascular endothelial (VE)-Cadherin stain.

2. Materials and methods

All chemicals, unless stated otherwise, were purchased from Sigma-Aldrich (Saint Luis, USA). The images were captured using a laser-scanning confocal microscope (LSM 800 Airyscan, Zeiss, Oberkochen, Germany).

2.1. Cell culture

ASC/TERT1 adipose derived stem cells and green fluorescent protein (GFP) labelled ASC/TERT1 cells (ASC-GFP) (Evercyte, Vienna, Austria) were cultured in EGM-2 cell culture medium (Lonza Group AP, Basel, Switzerland) supplemented with an additional 8% foetal bovine serum (FBS) to achieve 10% final concentration of FBS. HUVEC labelled with red fluorescent protein (RFP-HUVEC) (PeloBiotech GmbH, Plantegg, Germany) were maintained in EGM-2 cell culture medium supplemented with an additional 3% FBS to have a final concentration of 5%. All cell culture plastic flasks used for RFP-HUVECs were coated with quick coating solution (PeloBiotech GmbH) for 15 min before the seeding of cells. The cells were sustained at 37 °C and 5% CO_2 incubator. When cells reached 90% confluency, 0.05% Trypsin-EDTA was added for 3 min to detach the cells. The cells were then diluted with fresh cell culture media and placed in T75 flasks (Greiner Bio-1, Kremsmünster, Austria). RFP-HUVECs were used between passage 4 and 10.

2.2. Two-photon polymerization (2PP) setup

A tuneable femtosecond near infrared (NIR) laser (MaiTai eHP DeepSee, Spectra-Physics) with a pulse duration of 70 fs after the microscope objective (Plan-Apochromat, 10x/0.4, Olympus, Tokyo, Japan) and a repetition rate of 80 MHz was employed. The used setup is described elsewhere [18]. All experiments were performed at a central wavelength of 720–725 nm and with a writing speed of 1000 mm s^{-1} and line spacing of 0.5 μm [44]. To compensate for the RI mismatch of the immersion medium and the fabrication material the layer spacing was multiplied with the correction factor (c)

$$c = \frac{n_i}{n_m}$$

with n_i being the RI of the immersion medium and n_m the RI of the material.

2.3. Methylcellulose preparation

Methyl cellulose was sterilized by autoclaving before the addition of preheated EGM-2 medium at 60 °C in the concentration of 1.2 w v^{-1} %. The solution was stirred with a magnetic stirrer for 20–30 min at room temperature, then for 2 h at 4 °C. Afterwards, the solution was centrifuged for 2 h at 5000 g at 4 °C. The supernatant was transferred to a new falcon tube and stored at 4 °C. For further application, a 20 V% methyl cellulose solution in EGM-2 containing 5% FBS was used.

2.4. Cell spheroid formation

Microtissues 3D Petri Dish 81-well micro-moulds were used to form endothelial spheroids. 1 wt % agarose solution was prepared in sterile water and heated until it dissolved. Once it dissolved, the microtissue moulds were filled up with agarose and left until it solidified. Afterwards, the agarose moulds were equilibrated in phosphate buffered saline (PBS) for at least 2 h in 12-well plates (Greiner-Bio, Kremsmünster, Austria). RFP-HUVECs were trypsinized with 0.05% Trypsin-EDTA to detach and centrifuged for 5 min at 170 g before resuspending it in 20% methylcellulose solution at a concentration of 8.1×10^4 cells per 300 µL. 300 µL of cell solution was pipetted on top of each agarose mould and left to sediment for at least 15 min before the addition of 2 ml of 20% methylcellulose solution in cell culture media. Spheroids were formed and used after 24 h. ASC-GFP spheroids were prepared using the same protocol without the addition of 20% methyl cellulose solution to their corresponding cell culture media.

2.5. Synthesis of gel-NB and gel-SH

The synthesis of Gel-NB was performed via reaction of 5-norbornene-2-carboxylic acid with the primary amines of gelatin type B (kindly supplied by Rousselot, Ghent, Belgium) using EDC (1–ethyl–3–(3–dimethylaminopropyl)carbodiimide; NHS (n-hydroxysuccinimide; Acros, Geel, Belgium) coupling chemistry according to a previously reported protocol yielding a degree of substitution (DS) of 90%. The Gel-SH was prepared via reaction of the primary amines with D,L-N-acetylhomocysteine thiolactone yielding a DS of 63% [13, 45].

2.6. Functionalization of the high precision glass slides

In order to improve the adhesion of the produced hydrogel structures on the chip, the 170 μm thick glass coverslips (IBIDI GmbH, Martinsried, Germany) were functionalised. To this end, they were plasma cleaned for 10 min. Subsequently, 10 vol % of (3-mercaptopropyl)trimethoxysilane was mixed with 85.5% ethanol and 4.5% deionized water and the plasma cleaned coverslips were submerged for 3 h at room temperature. Afterwards, the glass slides were washed three times with ethanol on both sides and were dried under nitrogen gas. Finally, they were placed in a heating chamber at 110 °C for 10 min. All functionalized coverslips were stored in ethanol until use.

2.7. UV-induced cell encapsulation

Gel-SH and Gel-NB based hydrogels were prepared by dissolving them in phosphate buffered saline (PBS) in a 37 °C water bath. Once dissolved, the two components were mixed to achieve a final concentration of 5 wt% at an equimolar thiol/ene ratio. For the single cell suspension sample, RFP-HUVECs were trypsinized and resuspended in a final concentration of 8.1×10^5 cells per ml together with a single suspension of ASC/TERT1 cell at a 1:1 ratio in respect of the cell number. The cell suspension was added to the hydrogel precursor solution together with 0.3 mM Li-TPO photoinitiator [46] and 30 μl of the hydrogel-precursor mixture was pipetted on functionalized glass bottom dishes (IBIDI, GmbH) followed by UV irradiation at 365 nm at 1 J (Boekel Scientific UV Crosslinker AH, USA). For the spheroid experiments, RFP-HUVEC spheroids were removed from the agarose mould and mixed with a single cell suspension of ASC/TERT1 cells in the above-mentioned concentration together with the hydrogel precursors and 0.3 mM Li-TPO followed by UV irradiation as described above. Finally, EGM-2 with 5% FCS cell culture medium was added to the hydrogel pellets. The hydrogel pellets were imaged for 5 days using LSM.

2.8. Dextran-FITC perfusion

After 5 days, the cell containing hydrogels were cut in half with a scalpel and 0.5 mg ml^{-1} 70 and 2000 kDa dextran-FITC (TdB Consultancy, Uppsala, Sweden) dissolved in cell culture media was added. The diffusion of the dextran was recorded using LSM 800 after 1 h of incubation at 37 °C (figure S1).

2.9. Voxel simulation

Due to the nonlinear nature of 2PP, considerations regarding the shape and size of the voxel can be done with the help of the squared illumination point spread function, IPSF$^2{}_{(x,y,z)}$, which describes the intensity distribution around the focus [47]. To simulate the point-spread function IPSF^2 for 2PP, the IPSF which describes one-photon absorption was first calculated with PSFLab [48]. The simulations were done in the xz-plane for an air objective ($n_1 = 1$) with a numerical aperture (NA) of 0.4 illuminated with a Gaussian beam propagating in z-direction with light polarized along the x direction at a wavelength (λ) of 720 nm with a filling factor (β_G) of 1. The coverslip was 170 μm thick with a RI of 1.52 (n_2). The simulated sample had a RI of 1.346 (n_3) for unpolymerized material and 1.356 for polymerized one based on a RI measurement on UV-crosslinked and precursor material using a refractometer (Zeiss, Oberkochen, Germany) The IPSF^2 was simulated for three different depths in the material.

The full width half maximum (FWHM) of the IPSF^2 was calculated with the values of the IPSF from the PSFLab simulations based on the FWHM of a gaussian function with

$$FWHM_{IPSF^2} = FWHM_{IPSF}\frac{1}{\sqrt{2}}$$

To calculate the intensity in the focal plane (I_{peak}), the laser pulse was assumed to be sech^2 (squared hyperbolic secant) shaped and the peak intensity was calculated with gaussian beam approximations using [49]

$$I_{peak} = 0.88\frac{P\pi(NA)^2}{R\tau_p\lambda^2}$$

With the average laser power (P), the NA of the objective, repetition rate (R) and the pulse duration (τ_p).

2.10. CAD-CAM mimicry quantification

The thiol-ene gelatin hydrogel was prepared by separately dissolving Gel-SH and Gel-NB in PBS at 37 °C. Once dissolved, the two components were mixed to achieve a final gelatin concentration of 7.5 wt % (1:1 thiol-ene ratio) and supplemented with 0.5 mM biocompatible diazosulphonate two-photon photoinitiator (DAS) [42]. For physical gelation, the samples were incubated at 8 °C for 15 min prior to printing. To quantify the aberrations, 500 μm x 500 μm x 500 μm cubes containing 30 μm rectangular channels at different heights were produced with the previously mentioned setup (figure 1(A)). After structuring, the residual material was removed by washing with warm PBS (37 °C) followed by overnight incubation at 37 °C to reach equilibrium swelling. The next day, the structures were incubated in PBS containing 2000 kDa

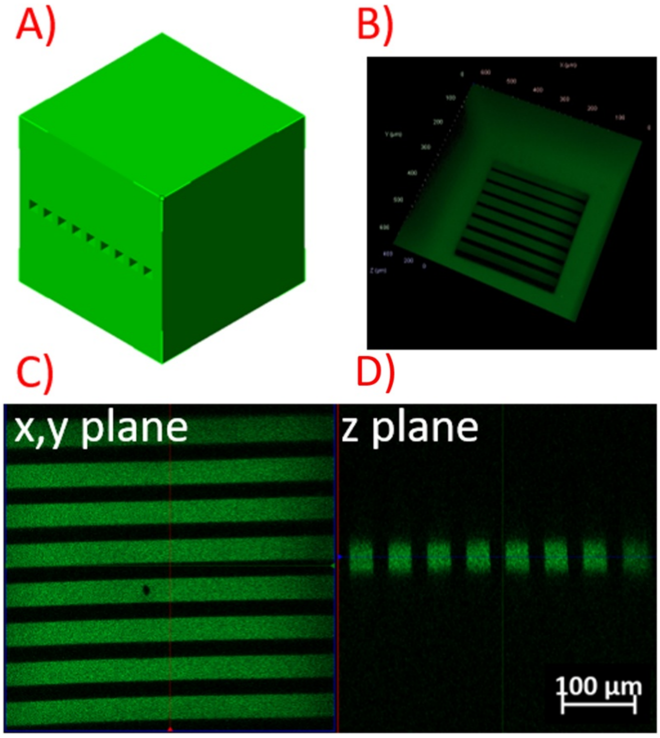

Figure 1. Quantitative measurement of CAD-CAM mimicry. (A) Representative CAD design of a single channel construct. (B) HD bioprinted design where the channels were filled with 2000 kDa FITC-dextran (C-D) The 2D images of the channels used for analysis at xy and z plane.

FITC-dextran and the diameter of the channels was imaged using LSM 800 (figure 1(B)). The images were analyzed using ImageJ and the channel diameters in xy and z plane direction were compared to the diameters of the designed CAD described in figures 1(C)–(D).

2.11. High-definition (HD) bioprinting of cell-containing constructs

After functionalization of the glass coverslips, a self-adhesive 6 channel slide (sticky-Slide VI 0.4, IBIDI GmbH, Germany) was mounted on the glass slide and was used immediately. The thiol-ene gelatin hydrogel was prepared by separately dissolving Gel-SH and Gel-NB in PBS at 37 °C. Once dissolved, the two components were mixed to achieve a final gelatin concentration of 7.5 wt% (1:1 thiol-ene ratio). The spheroids and the supporting cells were added based on the above described protocol. Finally, 0.5 mM DAS was added and the bioink was pipetted on the chip (approximately 30 μl). After printing, EGM-2 with 5% FBS cell culture media was added to the vessel constructs and the unpolymerized material was removed. Two days after printing, the samples were perfused with cell culture medium using a syringe pump (PHD Ultra, Harvard Apparatus, Cambridge, MA, USA) at a flow rate of 5 μl min^{-1} for an additional 3 days before fixing the cells.

2.12. Immunostaining

At different time points after printing, the constructs were washed with PBS and fixed for 2 h with 4% Histofix (Carl Roth GmbH, Karlsruhe, Germany). Afterwards, the fixed structures were washed with PBS and permeabilized with 0.5% Triton-X in PBS for 10 min. The non-specific absorption of the antibodies was blocked by incubation in 1 wt% bovine serum albumin in PBS (PBS-BSA) for 15 min before the addition of anti-VE Cadherin antibodies (Thermo-Fisher, Waltham, MA, USA) in a 1:500 dilution for 2 h at room temperature. Afterwards, the constructs were washed for 15 min with PBS-BSA before the addition of the Goat anti-Rabbit IgG Superclonal Secondary Antibody, Alexa Fluor 488 (Thermo-Fisher, Waltham, MA, USA) in a dilution of 1:1000 for 2 h. Next, the structures were washed again for 15 min with PBS-BSA before the addition of Hoechst 34 850 (Invitrogen, Carlsbad, CA, USA) in a dilution of 1:100 in PBS-BSA for 1 h. The cells were imaged using LSM 800.

2.13. HD bioprinting of intertwining spiral network

The thiol-ene gelatin hydrogel was prepared and 2PP-processed using the protocol described above. The produced structures were washed and developed using EGM-2 medium supplemented with 5% FCS and left to reach equilibrium swelling at 37°C. The RFP-HUVEC and ASC-GFP spheroids were

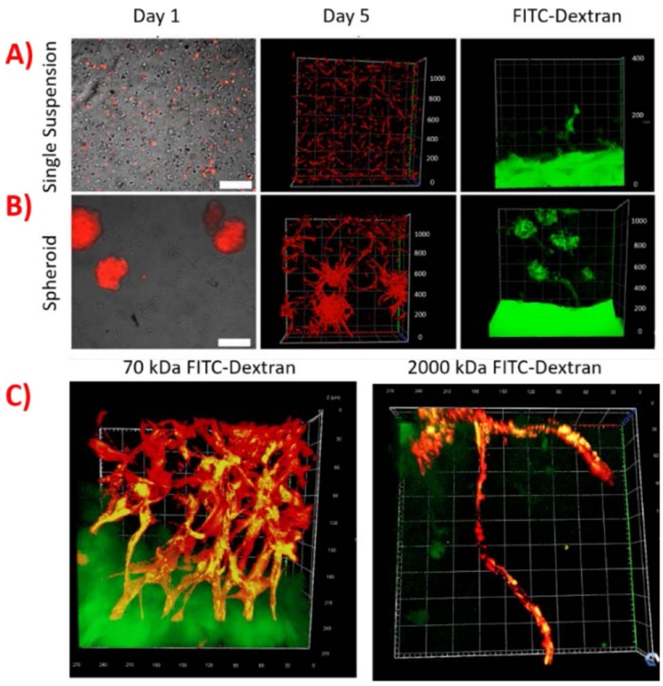

Figure 2. UV encapsulation of RFP-HUVEC and ASC/TERT1 cells in 5% Gel-SH and Gel-NB hydrogels. (A) Single cell suspension of RFP-HUVECs and unlabelled ASC/TERT cells encapsulated at 1:1 ratio. The red fluorescent protein label allows the direct imaging of the cells without the need of further staining, while the ASC/TERT1 supporting cell line is only visible under bright field microscopy. After day 5, the RFP-HUVECs shows extended morphology, although the cells stayed separated without the formation of a preliminary network. Upon incubation with 2000 kDa dextran-FITC after 5 days the dye was only able to diffuse into the hydrogel up to 100 μm after 1 h. (B) RFP-HUVECs spheroid co-culture with ASC/TERT1 supporting cells. After UV-induced encapsulation, the spheroids showed a round morphology. However, after 5 days, the cells started to sprout from the spheroid towards each other showing a higher degree of interconnection within the hydrogel. When incubating with 2000 kDa dextran-FITC, the dye was able to penetrate the hydrogel fully after 1 h. (C) Co-localization of the FITC-dextran with RFP-HUVEC spheroid networks using 70 kDa and 2000 kDa dextran after 5 days.

removed from the mould by pipetting and were drop-seeded at the opposite sides of the chip. The system was monitored for 5 days using LSM 800.

3. Results and discussion

3.1. UV embedding of RFP-HUVECs with supporting cells in thiol-ene hydrogel

Thiol-ene photo-click gelatin hydrogels already showed remarkably high processability, biocompatibility and supported the adhesion and proliferation of cells when used as a bioink for HD bioprinting [18]. In order to assess the capacity of RFP-HUVEC to form preliminary vascular networks in a Gel-NB-Gel-SH hydrogel, the cells were first encapsulated via UV-induced crosslinking. To this end, (ASC/TERT1) were used in a 1:1 ratio to the HUVECs as supporting cells.

Previous studies have highlighted the importance of high initial cell loading and cell-cell contact for vascularization [50]. Therefore, two different settings, namely a single cell suspension and a spheroid culture of RFP-HUVECs were compared to investigate the influence of spheroid culture on network formation. The spheroids were obtained overnight after seeding the cells onto non-adhesive agarose moulds and were encapsulated via UV-induced encapsulation in 5 wt% Gel-NB-Gel-SH hydrogels at an equimolar thiol/ene ratio in the presence of 0.3 mM UV photoinitiator (i.e. Li-TPO) and the supporting cells. After UV encapsulation, the cells were imaged at different time points using LSM. Due to the red fluorescent label, the RFP-HUVECs are visible without staining, while the supporting cells are not interfering with the imaging of the network. In both cases, the thiol-ene photo-click Gel-NB-Gel-SH showed good biocompatibility and supported cell survival and adhesion. Although the cells were characterized by a uniform cell distribution and good cell viability immediately after encapsulation, the single cell suspension did not show any sign of interconnection between the cells after 5 days despite the fact that the cells exhibited an elongated morphology. Previous studies have employed fluorescently labelled dextran (FITC-dextran) to evaluate the permeability of the preliminary vascular networks [51, 52]. When the diffusion of different sized dextran molecules was monitored on a monolayer of HUVECs using a transwell setup, the diffusion decreased with increasing molar mass, where the 2000 kDa dextran resulted in a diffusion rate close to zero after 2 h [53]. Since this high molar mass FITC-dextran is unable to diffuse into the bulk hydrogel, we hypothesize that it can only be detected across the matrix if a preliminary HUVECs aligned network is present, while the lower molecular weight FITC-dextran (70 kDa) which can also diffuse into the bulk of the hydrogel will also be traced within the capillaries which will be faster compared to the passive diffusion. Therefore, after 5 days, the hydrogel pellets containing cells were incubated with 2000 kDa dextran-FITC for 1 h to address the permeability of the system. After 1 h, the signal of the FITC-dextran could only be detected up to 100 μm from the edge of the hydrogel pellet (figure 2(A)). The spheroid co-culture however, presented a higher degree of sprouting after 5 days of co-culture with ASC/TERT1 cells. These cells exhibited an extended morphology as well. After incubation with the 2000 kDa dextran-FITC dye, it was possible to trace the fluorescence all across the hydrogel pellet after 1 h in which the FITC dextran showed co-localization with the HUVECs (figures 2(B)–(C)). Additionally, 70 kDa FITC-dextran, which can freely diffuse into the hydrogel, can be further along the network formed by HUVECs compared to the passive diffusion into the hydrogel (figure 2(C)).

3.2. Printing parameter optimization of small diameter channels

In order to fabricate reproducible organ- or tissue-on-chip models, having only randomly distributed microvascular network is often not satisfactory, as a precise positioning of the vascular network is also desired. However, most of the available biofabrication methods do not offer the resolution which allows the production of such small diameter round and branching channels [54, 55]. The accuracy of HD bioprinting depends on several different parameters which could be of crucial importance when producing these structures.

Especially important in this respect is to take into account the dimensions of the polymerized voxel during the printing process. The shape of the voxel resembles a spinning ellipsoid with the z axis being larger than the x and y planes. The size of the voxel is dependent on the NA of the objective, the RI of the material and the applied wavelength (λ) as described by equation(1) for the full width at half maximum (FWHM) of the voxel intensity in the x,y-plane and equation(2) for the z-plane [47].

$$FWHM_{x,y} = \frac{0.32\lambda}{\sqrt{2}NA} 2\sqrt{\ln 2} \tag{1}$$

$$FWHM_z = \frac{0.532\lambda}{\sqrt{2}} \left[\frac{1}{RI - \sqrt{RI^2 - NA^2}} \right] 2\sqrt{\ln 2} \tag{2}$$

The deeper the laser is focused in the material after the coverglass, the more spherical aberrations affect the voxel shape. The spherical aberration of the voxel during structuring was modelled using PSFlab with a custom-made algorithm. Figures 3(A)–(C) shows the simulation of the squared illumination point-spread function (IPSF^2) at different focusing depths. When structuring deeper into the material, the FWHM (table 1) increases, showing a larger focus area which results in a lower peak intensity and photon density in the focal area. These parameters could impact the accuracy of HD bioprinted structures leading to poor CAD-CAM mimicry.

Table 1. FWHM for x and z (beam propagation)-direction of the simulated IPSF^2 at different depths in the material.

Depth [μm]	FWHMx,y[μm]	FWHMz [μm]
0	0.731	7.628
100	0.734	7.856
400	0.903	14.949

During 2PP, the structures are formed by stacking of the voxels, therefore, their optimal arrangement is crucial for introducing high resolution features. The calculated voxel height of our setup at a depth between 0 and 100 μm is around 8 μm (table 1) when using a gelatin hydrogel (RI of unpolymerized material is approximately: 1.34, NA of the objective: 0.4, structuring wavelength: 720 nm), and supposing that the polymerized voxel corresponds to its FWHM. Although the influence of spherical aberrations on voxel height is negligible in smaller objects, it is more pronounced in higher structures as described in table 1. The simulated voxel height only shows a slight variation between focussing of the laser into polymerized or un-polymerized material (**table S1** available online at stacks.iop.org/BF/13/015016/mmedia). In order to provide a flexible possibility to account for variable voxel heights, a voxel compensation feature was introduced in the system control software. This feature allows the calculation of the laser irradiation path considering voxel height and the ratio in which the voxel would overlap with the designed channel. Once the object is sliced and overlap is detected, the voxel is left out during the printing process. For testing this printing mode, a cube containing several different sized round channels with diameters ranging from 10 to 30 μm was designed (figure 3(D)). This structure was either produced without setting the voxel height or overlap features (figure 3(E)) or with a voxel compensation of 8 μm (figure 3(F)). As the smallest feature size of the designed CAD is almost the same size as the voxel itself (10 μm), and every voxel which overlaps the channel by 0.2 was left out when processing the material. By adding this factor alone, it was possible to produce accurate channels within the 180 μm high cube.

Previous studies have shown that the surface roughness and accuracy of the 2PP structures are highly dependent on the voxel overlap settings (layer

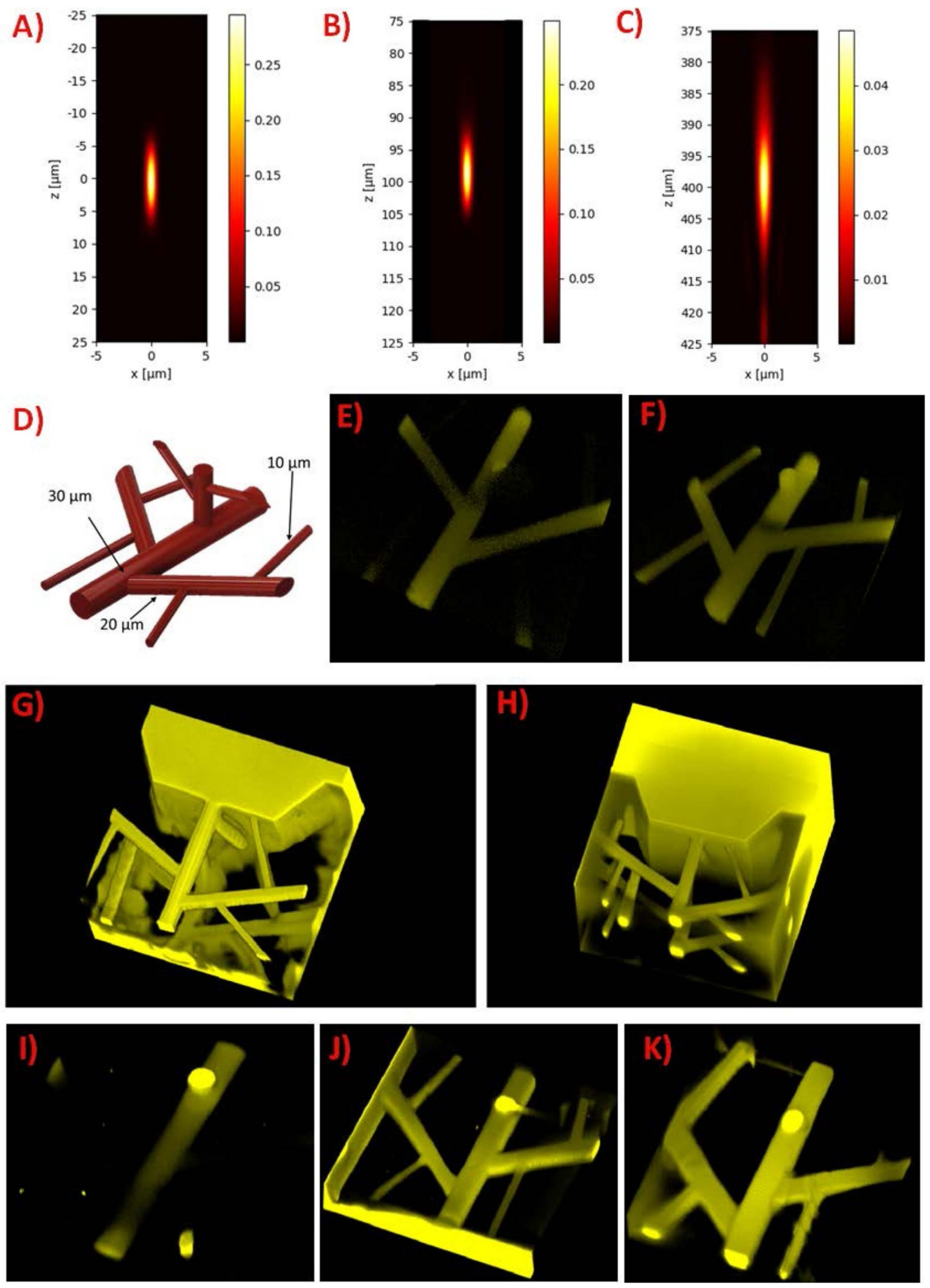

Figure 3. The accuracy and optimization of produced HD bioprinted small channelled structures. (A)–(C) Simulation of the IPSF^2 in the x,z plane at 720 nm. The IPSF^2 was simulated for three different positions in the material to show its distortion for increased structuring depths leading to a larger voxel. (A) IPSF^2 at the interface between coverslip and sample material at (B) 100 μm and (C) 400 µm depth in the sample material. (D)–(F) The effect of voxel compensation of the channelled structures of 180 µm height. (D) The designed CAD model containing branching round channels with different diameters ranging from 10–30 μm. (E) Structure produced without voxel compensation (F) with compensation for an 8 µm long voxel. (G)-(H) Optimization of structures with a height of 420 μm. (G) Structures produced bottom-up (BU), starting from the glass coverslip and (H) same structures produced top-down starting from the top of the microfluidic chip. (I)-(K) The effect of different layer spacing on the accuracy of the produced structure using 70 mW laser power and a voxel height of 8 μm (I) with a layer spacing of 0.5 μm (J) layer spacing of 3 μm (K) layer spacing of 9 μm.

spacing, dz) [43]. By increasing the overlap, surface roughness decreases thereby allowing the printing of well-defined features, however in turn it increases the structuring time. By increasing the laser power, the voxel size also increases in all dimensions [56]. In order to test the power dependency of the overlap setting, the previously mentioned cubes with different sized channels (figure 3) were produced at different powers (45 mW, 70 mW and 100 mW) with an increasing layer spacing from 0.5 μm to 13 μm using the previously described voxel intersection printing mode settings. The ability to perfuse the

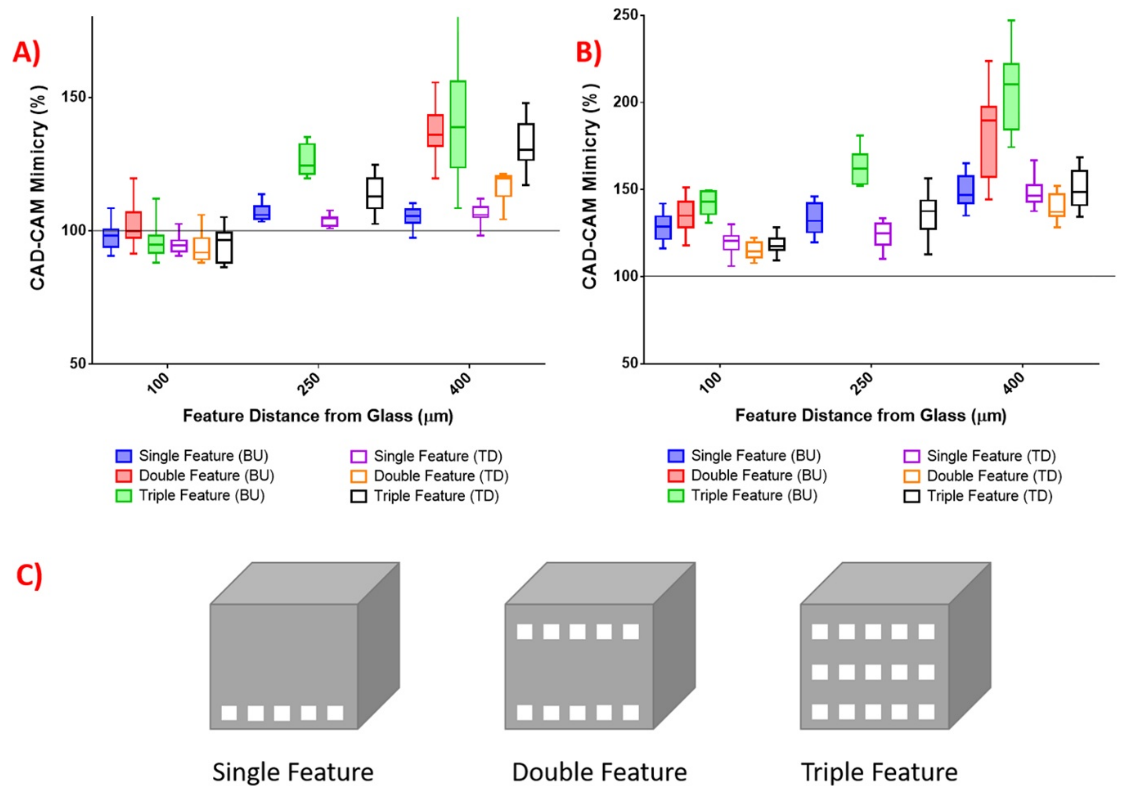

Figure 4. The reproducibility of channeled structures using different printing modes at XY and Z planes at different heights. (A) CAD-CAM mimicry at the XY plane using top-down and bottom-up printing modes. (B) CAD-CAM mimicry at the Z plane using top-down and bottom-up printing modes. (C) CAD-designs of channeled structures.

produced channels was set as a quality threshold in regard of over-polymerization and mechanical stability. Table 2 shows the used average powers (P_{avg}) with calculated peak intensities (I_{peak}) and the layer spacing ($d_{z_{th}}$) at which the channels were first perfusable (not over-polymerized). Since the area within the FWHM is mainly contributing to induce 2PP, the simulated FWHMz value at 100 µm depth at which the intensity has fallen to half of its value, was used as reference value. For a peak intensity of 686 GW cm^{-2}, z-distances between the voxels that were smaller than 25% of the FWHMz led to over-polymerization within the material, resulting in closed channels. Similar result was also observed at peak intensities of 1067 GW cm^{-2} and 1524 GW cm^{-2} for layer spacings of less than 38% and 89% of the FWHMz. When choosing small layer spacings, the number of voxels that overlap is increased and the structuring area is illuminated more often with the highly effective area around the focal spot, generating a higher number of radicals. Further, when structuring with smaller layer spacing, it is possible that parts of the voxel reach into the channels. We hypothesize that these two effects lead to over-polymerization of the material within the channels. When increasing the intensity, the voxel size is increased and so is the overlap region, which makes it necessary to increase the layer spacing. Figure 3(I) shows an example of over-polymerization at 70 mW with different layer spacings which is visualized in figures 3(I)–(K) with figure 3(I) at 0.5 μm, figure 3(J) at 3 μm and figure 3(K) at 9 μm overlap. By choosing the optimal layer spacing, the structuring time was reduced by 10-fold compared to previously reported protocols [18, 42]. With a layer spacing of 0.5 μm, the CAD depicted in figure 3(D) takes over 9 min to print, while when using a layer spacing of 5 μm, the same design takes less than 50 s while maintaining the round shape and accuracy of the channel.

Table 2. Average powers, peak intensities, intensities at FWHM$_z$ and threshold layer spacings allowing the production of open channels at different power settings.

P_{avg} [mW]	45	70	100
I_{peak} [GW cm^{-2}]	685.67	1066.59	1523.70
I_{FWHM} [GW cm^{-2}]	342.83	533.30	761.85
dz_{th} [μm]	1.5	3	7

Several previous studies indicated that forming a physical gel before processing can improve the mechanical stability and influence the properties of gelatin-based hydrogels [15, 57, 58]. This phenomenon is attributed to an improved crosslinking efficiency, as upon physical gelation interchain hydrogen bonds are formed in the gelatin backbone, leading to semi-crystalline junction zones which can be partially locked by covalent crosslinks, possibly resulting in closer proximity between crosslinkable groups [15, 58]. Additionally, even a small difference between the RI of the (glass) substrate and the material can

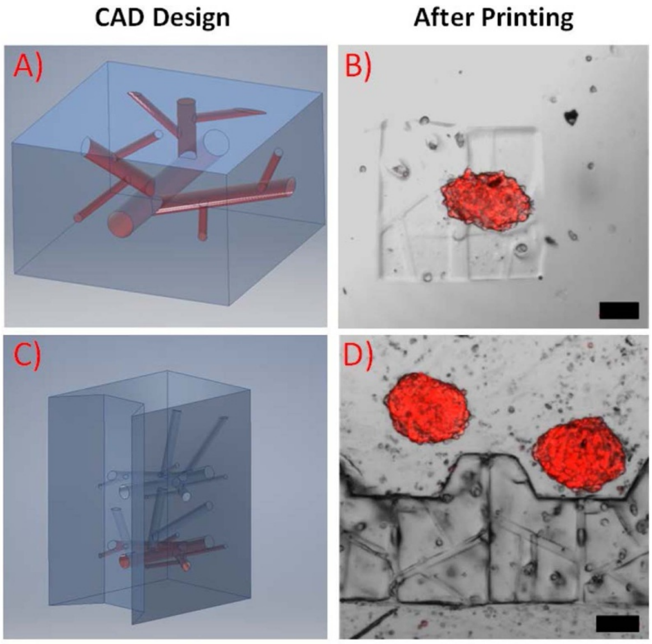

Figure 5. The two different chip setups tested for the vascular network formation of RFP-HUVECs. (A) CAD design of a single unit vessel with a height of 180 μm. (B) The produced structure, where both the supporting cells and the RFP-HUVECs were embedded in the hydrogel. (C) CAD design of a vessel barrier with a height of 400 μm. (D) Only the supporting cells were embedded during HD Biopriting and spheroids were added after developing the structure. The scale bars represent 100 μm.

lead to spherical aberrations which is mainly dependent on the difference in the refractive indices and the focusing depth [59]. In turn, these aberrations change the irradiation conditions and therefore lead to an inhomogeneous 2PP structuring at different sample depths. During 2PP from the cover glass into the material (BU), the objective has to focus through multiple interfaces of already polymerized material with different RI's leading to additional scattering of the light and further spherical aberrations, which in turn can result in a mechanically weaker and distorted structure. Therefore, two different 2PP modes, BU and top-down (starting from the top of the structure, TD) were tested.

In order to quantify the effect of physical pregelation and 2PP mode on the structuring integrity of produced constructs, 500 μm tall cubes containing channels with a diameter of 30 μm were produced TD and BU both in a physically gelled and non-gelled state using the previously established voxel intersection mode with a layer spacing of 5 μm. The cubes contained channels at different heights, either at 100 μm, 250 μm or 400 μm. Once the produced structures were developed and swollen overnight, the diameters of the channels were measured using Image J at both xy and in z planes and the CAD-CAM mimicry was plotted. Our results indicate that physical gelation does improve the reproducibility of the channels but it does *not* significantly differ from the non-gelled samples for both printing modes (figure S2(A) and figure S2(B)) possibly due to the high viscosity of the hydrogel at room temperature.

In order to test the effect of different printing modes on samples with multiple features, similar cubes containing multiple sets of channels at different heights were tested, where the double feature ones had a set of channels at 100 and 400 μm and triple feature samples at 100, 250 and 400 μm. Compared to BU mode, the TD mode consistently leads to better CAD-CAM mimicry by avoiding focussing through the non-uniform material containing 2PP structures already produced at different heights (figure 4). Close to the glass coverslip, the different printing modes did not show any significant differences independently of the number of features introduced to the structure. However, when the BU mode was employed, the spherical aberration was more pronounced the deeper into the material the objective was focussed. The CAD-CAM mimicry has further deteriorated when more features were introduced to the cube, while this effect was less significant in the case of TD printing both in XY (figures 4(A)) and Z plane (figure 4(B)). Finally, double featured channels for vascular structures were produced and the results indicated that by printing top-down, the accuracy of the structures can indeed be improved (figure 3(H)) when compared to a BU approach (figure 3(G)).

3.3. HD bioprinting of microcirculation-on-a-chip constructs

After optimization of the 2PP parameters of small channelled structures on chip, two different setups were created to test the vascular network formation of RFP-HUVECs. In the first setup, the single unit

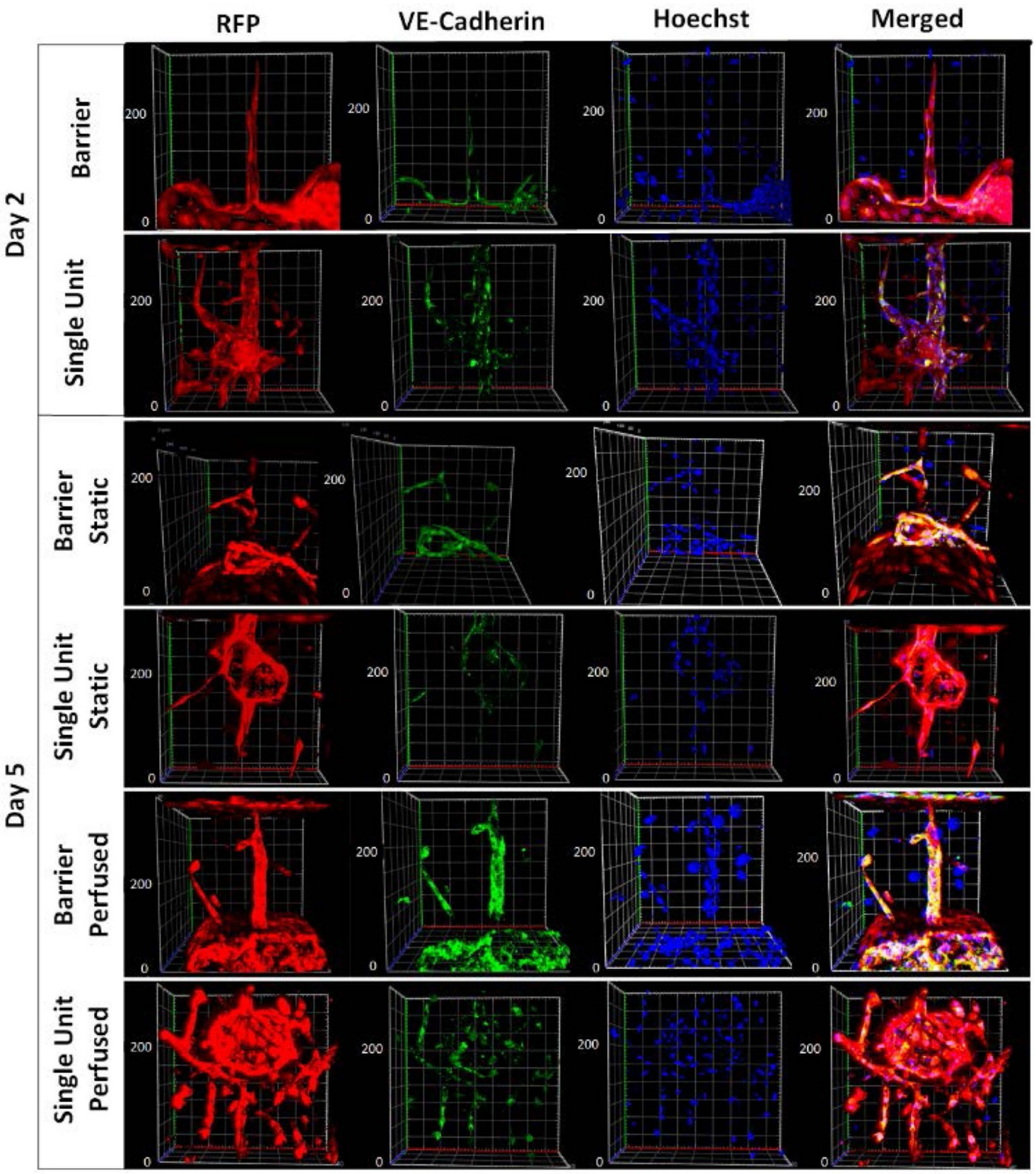

Figure 6. Immunostaining of vascular structures under different culturing conditions. The endothelial cells are visible via the red fluorescent protein label (RFP). The cells showed extended morphology even after 2 days post-printing. The endothelial vascular cadherin (VE-Cadherin) staining showed intercellular junction formation in all examined samples, however after 5 days, it was more pronounced at the perfused culture compared to the static samples. The cell nucleus was stained with Hoechst 34 850, showing a higher number of cells in the perfused culture compared to the static ones.

vessels (figure 5(A)), were produced by embedding both the supporting cells (ASC/TERT1) and the RFP-HUVECs in the bioink containing 7.5 wt% of the Gel-NB-Gel-SH hydrogel crosslinked with 0.5 mM DAS photo-initiator. During the 2PP process, a cube with a height of 180 μm and an internal channel structure was fabricated around the spheroid, positioning it in close proximity to the channels (figure 5(B)). Based on the previous experiments, the 2PP parameters were set at a laser power of 70 mW and a layer spacing of 5 μm using the voxel intersection mode. In the second setting, cubes with internal channels with a height of 400 μm were produced across the whole microfluidic channel thereby creating a barrier structure using the previously mentioned bioink formulation (figure 5(C)). In this case, only the supporting cells were embedded in the structure during the HD bioprinting process, as the spheroids in the bioink are randomly distributed. Consequently, positioning them close to the channels is not possible during the process. However, once the produced structure was developed by washing away the unpolymerized material, the RFP-HUVECs spheroids were drop-seeded to the created barrier, thereby allowing the migration of

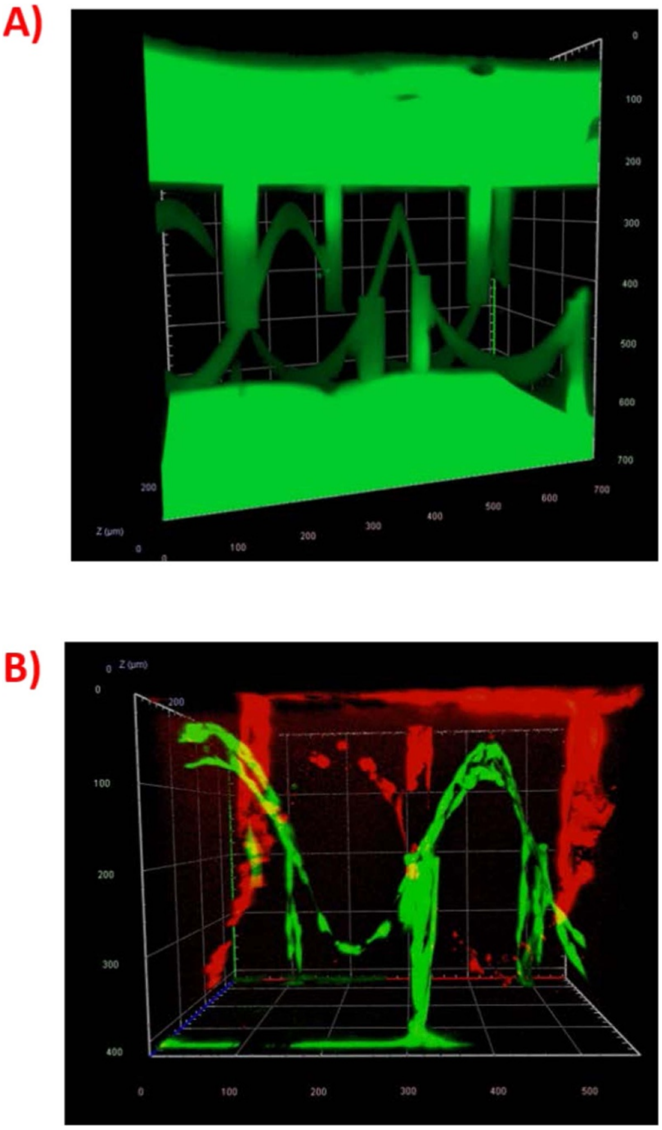

Figure 7. Intertwined spiral channels. (A) Produced sample perfused with 2000 kDa FITC-Dextran (B) ASC-GFP cell spheroids (green) and RFP-HUVECs entering the channels from two separate compartments after 5 days of culture.

the endothelial cells into the produced channels (figure 5(D)).

Previous studies have shown that HUVECs are responsive to glucose concentration and shear stress and that dynamic culture conditions increase the 3D organization of HUVECs into tubular structures when compared to a static environment [60–62]. We hypothesized that the introduction of perfusion to the microcirculation-on-a chip model would enhance cell survival and expression of cell adhesion molecules such as VE-Cadherin. To this end the produced structures were first incubated under static conditions for two days before the samples were perfused using a syringe pump at a flow rate of 5 μL min^{-1} for an additional three days. Next, the samples were fixed and co-stained with Hoechst 34 850 and VE-Cadherin. Cell adhesion molecules play an important role in the formation of neovascular networks during angiogenesis [63]. They are responsible for the formation of intercellular junctions between the endothelial cells, which are crucial to control the diffusion and transport of molecules and the endothelial surface polarity [64]. Previous studies have shown that VE-cadherin is one of the main endothelial specific cell adhesion molecules involved in vascular morphogenesis and growth control [65]. Even after two days of culture, the endothelial cells exhibited an extended morphology and were expressing VE-Cadherin at the barrier (figure 6**, first row**) as well as the single unit structure (figure 6**, second row).** As the endothelial cells were labelled with a red fluorescent protein, there was no need for further cell stains to visualize the cell body and morphology. The nuclear stain suggested cells both within the cube and also in the channels of the HD bioprinted constructs. After day 5, the static culture vessels showed less cells in both the barrier and single unit vessels, especially in the crosslinked regions when compared to the perfused culture according to the Hoechst staining, possibly due to the lack of constant nutrient supply and removal of metabolites. Additionally, the VE-Cadherin expression was more pronounced in the perfused culture as well, although the cell morphology remained extended in the static culture as well.

To further demonstrate the potential of our system and its capacity to create barrier structures using different cell types an intertwined spiral structure was produced (figure 7(A)) and GFP-labelled supporting cell spheroids (ASC-GFP) were seeded on one side whereas RFP-HUVECs spheroids were seeded on the opposite side of the chip. After 5 days of culture, the cells migrated into the produced spirals achieving an intertwined network of channels connected to two separated cell compartments (figure 7(B)), thereby demonstrating the high potential of the current methodology for the generation of vascular structures with a high degree of precision.

4. Conclusion

We have established and optimized the controlled HD bioprinting of small diameter branching channel networks based on Gel-NB-Gel-SH thiol-ene photo-click hydrogels directly on a chip in the presence of endothelial cell spheroids and supporting cells. We have demonstrated the capacity of these hydrogels to support endothelial cell adhesion and proliferation both in single cell suspension and spheroid culture via UV-induced encapsulation. Due to the more pronounced cell-cell interactions, the spheroid culture proved to be more efficient in network formation compared to the single cell suspension approach. A wide range of processing parameters were tested on small diameter channel structures in order to improve both the accuracy and the throughput of the printing process. The spherical aberrations caused by the RI mismatch and the focusing depth were modelled by a custom-made algorithm, and a voxel intersection strategy was developed to account for the voxel height in the printed structures.

Additionally, the two different printing modes, TD and BU approach were compared to further optimize the resolution of high structures. Different voxel overlaps and their dependency on the applied laser powers were compared both in terms of accuracy and also for the improvement of the structuring time. Further, the capacity of 2PP to create vascular structures within a microfluidic chip was tested with two different settings, first as a one-pot method, including both the supporting cells and the endothelial cell spheroids in the bioink, and as a supporting cell scaffold barrier to drop-seed the HUVECs spheroids after developing the structures. The functionality of the formed channels was demonstrated with immunostaining of VE-Cadherin endothelial adhesion molecules in both static and perfused culture. Finally, a structure containing complex intertwining channels was structured, followed by seeding of GFP-labelled HUVEC spheroids on one side and RFP-labelled ASC's on the other side, which showed to populated the channels, thereby demonstrating the great potential of HD bioprinting as a tool to guide cellular migration and blood vessel formation.

Acknowledgments

We would like to thank Professor Robert Liska and his group at the Institute of Applied Synthetic Chemistry of TU Wien for providing photoinitiators DAS and Li-TPO, Dr. Peter Gruber and Dr. Tommaso Zandrini for useful discussions. Funding from TU Biointerfaces Doctorate College, and the FWO-FWF grant (Research Foundation Flanders—Austrian Science Fund project) is gratefully acknowledged (FWOAL843, #I2444N28). JVH and LT hold an FWO-SB PhD grant (1S44016N and 1S26616N respectively) issued by the Research Foundation Flanders (FWO).

ORCID iDs

Sandra Van Vlierberghe
https://orcid.org/0000-0001-7688-1682
Aleksandr Ovsianikov
https://orcid.org/0000-0001-5846-0198

References

[1] Knight E and Przyborski S 2015 Advances in 3D cell culture technologies enabling tissue-like structures to be created *In Vitro J. Anat.* **227** 746–56

[2] Li Y and Kilian K A 2015 Bridging the Gap: from 2D cell culture to 3D microengineered extracellular matrices *Adv. Healthc. Mater.* **4** 2780–96

[3] Sosa-Hernández J E, Villalba-Rodríguez A M, Romero-Castillo K D, Aguilar-Aguila-Isaías M A, García-Reyes I E, Hernández-Antonio A, Ahmed I, Sharma A, Parra-Saldívar R and Iqbal H M N 2018 Organs-on-a-chip module: A review from the development and applications perspective *Micromachines* **9** 536

[4] Huh D, Hamilton G A and Ingber D E 2011 From 3D cell culture to organs-on-chips *Trends Cell Biol.* **21** 745–54

[5] Zhu J and Marchant R E 2011 Design properties of hydrogel tissue-engineering scaffolds *Expert Rev. Med. Devices* **8** 607–26

[6] Drury J L and Mooney D J 2003 Hydrogels for tissue engineering: scaffold design variables and applications *Biomaterials* **24** 4337–51

[7] Ullah F, Othman M B H, Javed F, Ahmad Z and Akil H M 2015 Classification, processing and application of hydrogels: A review *Mater. Sci. Eng.* C **57** 414–33

[8] Kular J K, Basu S and Sharma R I 2014 The extracellular matrix: structure, composition, age-related differences, tools for analysis and applications for tissue engineering *J. Tissue Eng.* **5** 204173141455711

[9] Glowacki J and Mizuno S 2008 Collagen scaffolds for tissue engineering *Biopolymers* **89** 338–44

[10] Antoine E E, Vlachos P P and Rylander M N 2015 Tunable collagen I hydrogels for engineered physiological tissue micro-environments *PLoS One* **10** 1–19

[11] Deng C, Li F, Hackett J M, Chaudhry S H, Toll F N, Toye B, Hodge W and Griffith M 2010 Collagen and glycopolymer based hydrogel for potential corneal application *Acta Biomater.* **6** 187–94

[12] Suri S and Schmidt C E 2009 Photopatterned collagen-hyaluronic acid interpenetrating polymer network hydrogels *Acta Biomater.* **5** 2385–97

[13] Van Vlierberghe S, Schacht E and Dubruel P 2011 Reversible gelatin-based hydrogels: finetuning of material properties *Eur. Polym. J.* **47** 1039–47

[14] Nikkhah M, Akbari M, Paul A, Memic A, Dolatshahi-Pirouz A and Khademhosseini A 2016 Gelatin-based biomaterials for tissue engineering and stem cell bioengineering *Biomater. Nat. Adv. Devices Ther.* (Hoboken, NJ: Wiley) pp 37–62

[15] Van Hoorick J, Tytgat L, Dobos A, Ottevaere H, Van Erps J, Thienpont H, Ovsianikov A, Dubruel P and Van Vlierberghe S 2019 Photo-)crosslinkable gelatin derivatives for biofabrication applications *Acta Biomater.* **97** 46–73

[16] Markovic M, Van Hoorick J, Hölzl K, Tromayer M, Gruber P, Nürnberger S, Dubruel P, Van Vlierberghe S, Liska R and Ovsianikov A 2015 Hybrid tissue engineering scaffolds by combination of three-dimensional printing and cell photoencapsulation *J. Nanotechnol. Eng. Med.* **6** 021004

[17] Fedorovich N E, Oudshoorn M H, van Geemen D, Hennink W E, Alblas J and Dhert W J A 2009 The effect of photopolymerization on stem cells embedded in hydrogels *Biomaterials* **30** 344–53

[18] Dobos A, Van Hoorick J, Steiger W, Gruber P, Markovic M, Andriotis A G, Rohatschek A, Rohatschek P, Thurner P, Van Vlierberghe S, Baudis S and Ovsianikov A 2020 Thiol–gelatin–norbornene bioink for laser-based high-definition bioprinting *Adv. Healthc. Mater.* **9** 1900752

[19] Rouwkema J, Rivron N C and van Blitterswijk C A 2008 Vascularization in tissue engineering *Trends Biotechnol.* **26** 434–41

[20] Kim J J, Hou L and Huang N F 2016 Vascularization of three-dimensional engineered tissues for regenerative medicine applications *Acta Biomater.* **41** 17–26

[21] Carmeliet P and Jain R K 2000 Angiogenesis in cancer and other diseases *Nature* **407** 249–57

[22] Yuan S Y and Rigor R R 2010 *Regulation of Endothelial Barrier Function* (San Rafael, CA: Morgan & Claypool Life Sciences)

[23] Burton A C 1954 Relation of structure to function of the tissues of the wall of blood vessels *Physiol. Rev.* **34** 619–43

[24] Patan S 2004 Vasculogenesis and angiogenesis *Cancer Treat. Res.* **117** 3–32

[25] Gafni Y, Zilberman Y, Ophir Z, Abramovitch R, Jaffe M, Gazit Z, Domb A and Gazit D 2006 Design of a filamentous polymeric scaffold for *in vivo* guided angiogenesis *Tissue Eng.* **12** 3021–34

[26] Druecke D, Langer S, Lamme E, Pieper J, Ugarkovic M, Steinau H U and Homann H H 2004 Neovascularization of poly(ether ester) block-copolymer scaffoldsin vivo: long-term investigations using intravital fluorescent microscopy *J. Biomed. Mater. Res.* **68A** 10–18

[27] Bishop E T, Bell G T, Bloor S, Broom I J, Hendry N F and Wheatley D N 1999 An in vitro model of angiogenesis: basic features *Angiogenesis* **3** 335–44

[28] Guzzardi M A, Vozzi F and Ahluwalia A D 2009 Study of the crosstalk between hepatocytes and endothelial cells using a novel multicompartmental bioreactor: a comparison between connected cultures and cocultures *Tissue Eng. Part* A **15** 3635–44

[29] Strassburg S, Nienhueser H, Björn Stark G, Finkenzeller G and Torio-Padron N 2016 Co-culture of adipose derived stem cells and endothelial cells in fibrin induces angiogenesis and vasculogenesis in a chorioallantoic membrane model *J. Tissue Eng. Regen. Med.* **10** 496–506

[30] Lozito T P, Kuo C K, Taboas J M and Tuan R S 2009 Human mesenchymal stem cells express vascular cell phenotypes upon interaction with endothelial cell matrix *J. Cell. Biochem.* **107** 714–22

[31] Kirkpatrick C J, Fuchs S and Unger R E 2011 Co-culture systems for vascularization — learning from nature *Adv. Drug Deliv. Rev.* **63** 291–9

[32] Kim S, Kim W, Lim S and Jeon J S 2017 Vasculature-on-a-chip for in vitro disease models *Boengineering* **4** 8

[33] Baker B M, Trappmann B, Stapleton S C, Toro E and Chen C S 2013 Microfluidics embedded within extracellular matrix to define vascular architectures and pattern diffusive gradients *Lab Chip* **13** 3246–52

[34] Chrobak K M, Potter D R and Tien J 2006 Formation of perfused, functional microvascular tubes in vitro *Microvasc. Res.* **71** 185–96

[35] Datta P, Ayan B and Ozbolat I T 2017 Bioprinting for vascular and vascularized tissue biofabrication *Acta Biomater.* **51** 1–20

[36] Zhang Y, Yu Y and Ozbolat I T 2013 Direct bioprinting of vessel-like tubular microfluidic channels *J. Nanotechnol. Eng. Med.* **4** 020902

[37] Bertassoni L E *et al* 2014 Hydrogel bioprinted microchannel networks for vascularization of tissue engineering constructs *Lab Chip* **14** 2202–11

[38] Norotte C, Marga F S, Niklason L E and Forgacs G 2009 Scaffold-free vascular tissue engineering using bioprinting *Biomaterials* **30** 5910–7

[39] Kucukgul C, Ozler S B, Inci I, Karakas E, Irmak S, Gozuacik D, Taralp A and Koc B 2015 3D bioprinting of biomimetic aortic vascular constructs with self-supporting cells *Biotechnol. Bioeng.* **112** 811–21

[40] Ovsianikov A, Khademhosseini A and Mironov V 2018 The synergy of scaffold-based and scaffold-free tissue engineering strategies *Trends Biotechnol.* **36** 348–57

[41] Ovsianikov A, Mühleder S, Torgersen J, Li Z, Qin X H, Van Vlierberghe S, Dubruel P, Holnthoner W, Redl H, Liska R and Stampfl J 2014 Laser photofabrication of cell-containing hydrogel constructs *Langmuir* **30** 3787–94

[42] Tromayer M, Dobos A, Gruber P, Ajami A, Dedic R, Ovsianikov A and Liska R 2018 A biocompatible diazosulfonate initiator for direct encapsulation of human stem cells *via* two-photon polymerization *Polym. Chem.* **9** 3108–17

[43] Zhou X, Hou Y and Lin J 2015 A review on the processing accuracy of two-photon polymerization *AIP Adv.* **5** 030701

[44] Steiger W, Gruber P, Theiner D, Dobos A, Lunzer M, Van Hoorick J, Van Vlierberghe S, Liska R and Ovsianikov A 2019 Fully automated z-scan setup based on a tunable fs-oscillator *Opt. Mater. Express* **9** 3567

[45] Van Hoorick J *et al* 2018 Highly reactive thiol-norbornene photo-click hydrogels: towards improved processability *Macromol. Rapid Commun.* **39** 1800181

[46] Benedikt S, Wang J, Markovic M, Moszner N, Dietliker K, Ovsianikov A, Grützmacher H and Liska R 2016 Highly efficient water-soluble visible light photoinitiators *J. Polym. Sci.* A **54** 473–9

[47] Zipfel W R, Williams R M and Webb W W 2003 Nonlinear magic: multiphoton microscopy in the biosciences *Nat. Biotechnol.* **21** 1369–77

[48] Nasse M J and Woehl J C 2010 Realistic modeling of the illumination point spread function in confocal scanning optical microscopy *J. Opt. Soc. Am.* A **27** 295

[49] Zhang B, Zerubia J and Olivo-Marin J-C 2007 Gaussian approximations of fluorescence microscope point-spread function models *Appl. Opt.* **46** 1819

[50] Laschke M W and Menger M D 2017 Spheroids as vascularization units: from angiogenesis research to tissue engineering applications *Biotechnol. Adv.* **35** 782–91

[51] Pauty J, Usuba R, Takahashi H, Suehiro J, Fujisawa K, Yano K, Nishizawa T and Matsunaga Y T 2017 A vascular

permeability assay using an in vitro human microvessel model mimicking the inflammatory condition *Nanotheranostics* **1** 103–13

[52] Miyazaki K, Hashimoto K, Sato M, Watanabe M, Tomikawa N, Kanno S, Kawasaki Y, Momoi N and Hosoya M 2017 Establishment of a method for evaluating endothelial cell injury by TNF-α in vitro for clarifying the pathophysiology of virus-associated acute encephalopathy *Pediatr. Res.* **81** 942–7

[53] Nevo N, Chossat N, Gosgnach W, Logeart D, Mercadier J J and Michel J B 2001 Increasing endothelial cell permeability improves the efficiency of myocyte adenoviral vector infection *J. Gene Med.* **3** 42–50

[54] Miri A K, Mirzaee I, Hassan S, Mesbah Oskui S, Nieto D, Khademhosseini A and Zhang Y S 2019 Effective Bioprinting Resolution in Tissue Model Fabrication *Lab Chip* **19** 2019–37

[55] Murphy S V and Atala A 2014 3D bioprinting of tissues and organs *Nat. Biotechnol.* **32** 773–85

[56] Sun H-B, Takada K, Kim M-S, Lee K-S and Kawata S 2003 Scaling laws of voxels in two-photon photopolymerization nanofabrication *Appl. Phys. Lett.* **83** 1104–6

[57] Billiet T, Gevaert E, De Schryver T, Cornelissen M and Dubruel P 2014 The 3D printing of gelatin methacrylamide cell-laden tissue-engineered constructs with high cell viability *Biomaterials* **35** 49–62

[58] Van Hoorick J, Gruber P, Markovic M, Tromayer M, Van Erps J, Thienpont H, Liska R, Ovsianikov A, Dubruel P and Van Vlierberghe S 2017 Cross-linkable gelatins with superior mechanical properties through carboxylic acid modification: increasing the two-photon polymerization potential *Biomacromolecules* **18** 3260–72

[59] Booth M J and Wilson T 2001 Refractive-index-mismatch induced aberrations in single-photon and two-photon microscopy and the use of aberration correction *J. Biomed. Opt.* **6** 266

[60] Lovecchio J, Pannella M, Giardino L, Calzà L and Giordano E 2020 A dynamic culture platform enhances the efficiency of the 3D HUVEC-based tube formation assay *Biotechnol. Bioeng.* **117** 789–97

[61] Patel H, Chen J, Das K C and Kavdia M 2013 Hyperglycemia induces differential change in oxidative stress at gene expression and functional levels in HUVEC and HMVEC *Cardiovasc. Diabetol.* **12** 1–14

[62] Walshe T E, Dela Paz N G and D'Amore P A 2013 The role of shear-induced transforming growth factor-β signaling in the endothelium *Arterioscler. Thromb. Vasc. Biol.* **33** 2608–17

[63] Brooks P C 1996 Cell adhesion molecules in angiogenesi *Cancer Metastasis Rev.* **15** 187–94

[64] Brinkmann B F, Steinbacher T, Hartmann C, Kummer D, Pajonczyk D, Mirzapourshafyi F, Nakayama M, Weide T, Gerke V and Ebnet K 2016 VE-cadherin interacts with cell polarity protein Pals1 to regulate vascular lumen formation *Mol. Biol. Cell* **27** 2811–21

[65] Lampugnani M G and Dejana E 1997 Interendothelial junctions: structure, signalling and functional roles *Curr. Opin. Cell Biol.* **9** 674–82